Nanoscale Nuclear Magnetic Resonance with a Nitrogen-Vacancy Spin Sensor

H. J. Mamin *et al.*

Science **339**, 557 (2013);
DOI: 10.1126/science.1231540

Science (print ISSN 0036-8075; online ISSN 1095-9203) is published weekly, except the last week in December, by the American Association for the Advancement of Science, 1200 New York Avenue NW, Washington, DC 20005.

cesium atoms ω_{Cs}. This yields its mass as $M = \omega_M \hbar / c^2$. The ratio $m(\mathrm{Si})/m(^{133}\mathrm{Cs})$ is between the effective molar mass of the sphere's material and cesium-133. According to (*25*), present data yields the spheres' mass with an overall accuracy of 30 ppb so that they would constitute the most accurately calibrated macroscopic masses under the proposed CGPM-2011 redefinition—a testament to the precision achieved in constructing Avogadro spheres.

Although any method for measuring microscopic mass can be used, the Compton clock offers a transparent connection between the second and a microscopic mass on the basis of simple physical principles without requiring auxiliary measurements. It directly realizes a long-standing proposal to measure mass in terms of the Compton frequency (*6*). The method outlined here offers a different set of systematic effects as compared with Watt balances (*23*, *24*), thus serving as an important test of the overall consistency of the laws of physics and experimental methods. It is based on a body's inertial rather than gravitational mass. In the context of the present SI, the combination of the Avogadro project and the Compton clock serves as a measurement of the Planck constant.

Looking forward, the rapidly developing field of optomechanics (*26*) might enable measurements of the single-photon recoil energy of a nanomechanical mirror. This could result in a clock referenced to the mass of a mesoscopic object, or a mesoscopic mass standard. Because Bragg diffraction of electrons has already been demonstrated (*27*), a clock using elementary particles or even antiparticles is possible. Such clocks would be useful for testing CPT symmetry or the Einstein Equivalence Principle for antimatter.

We have demonstrated a clock stabilized to the rest mass of a particle. It highlights the intimate connection between frequency and mass. It proves that massive particles can serve as a frequency reference without requiring their mass to be converted to energy as an explicit illustration of a key principle of quantum mechanics. Furthermore, we have shown that a single massive particle is sufficient to measure time.

References and Notes

1. R. Penrose, *Cycles of Time: An Extraordinary View of The Universe* (Knopf, New York, 2011), sec. 2.3.
2. L. De Broglie, thesis, University of Paris, Paris, France (1924).
3. H. Müller, A. Peters, S. Chu, *Nature* **463**, 926 (2010).
4. M. A. Hohensee, S. Chu, A. Peters, H. Müller, *Phys. Rev. Lett.* **106**, 151102 (2011).
5. P. Wolf *et al.*, *Class. Quantum Gravity* **28**, 145017 (2011).
6. J. W. G. Wignall, *Phys. Rev. Lett.* **68**, 5 (1992).
7. Ch. J. Bordé, *Eur. Phys. J. Spec. Top.* **163**, 315 (2008).
8. M. A. Hohensee, B. Estey, P. Hamilton, A. Zeilinger, H. Müller, *Phys. Rev. Lett.* **108**, 230404 (2012).
9. L. Essen, J. V. L. Parry, *Nature* **176**, 280 (1955).
10. T. E. Parker, *Metrologia* **47**, 1 (2010).
11. A. D. Ludlow *et al.*, *Science* **319**, 1805 (2008).
12. C. W. Chou, D. B. Hume, J. C. J. Koelemeij, D. J. Wineland, T. Rosenband, *Phys. Rev. Lett.* **104**, 070802 (2010).
13. A. D. Cronin, J. Schmiedmayer, D. E. Pritchard, *Rev. Mod. Phys.* **81**, 1051 (2009).
14. H. Müller, S.-W. Chiow, Q. Long, S. Herrmann, S. Chu, *Phys. Rev. Lett.* **100**, 180405 (2008).
15. S.-Y. Lan, P.-C. Kuan, B. Estey, P. Haslinger, H. Müller, *Phys. Rev. Lett.* **108**, 090402 (2012).
16. Materials and methods are available as supplementary materials on *Science* Online.
17. R. Bouchendira, P. Cladé, S. Guellati-Khélifa, F. Nez, F. Biraben, *Phys. Rev. Lett.* **106**, 080801 (2011).
18. P. J. Mohr, B. N. Taylor, D. B. Newell, *The 2010 CODATA Recommended Values of the Fundamental Physical Constants* (Web Version 6.0); http://physics.nist.gov/constants.
19. S. Dimopoulos, P. W. Graham, J. M. Hogan, M. A. Kasevich, *Phys. Rev. Lett.* **98**, 111102 (2007).
20. "Resolution 1: On the possible future revision of the International System of Units, the SI," General Conference on Weights and Measures, Sèvres, France, 17 to 21 October 2011.
21. D. Hanneke, S. Fogwell, G. Gabrielse, *Phys. Rev. Lett.* **100**, 120801 (2008).
22. T. Aoyama, M. Hayakawa, T. Kinoshita, M. Nio, *Phys. Rev. Lett.* **109**, 111807 (2012).
23. I. A. Robinson, B. P. Kibble, *Metrologia* **44**, 427 (2007).
24. R. L. Steiner, E. R. Williams, R. Liu, D. B. Newell, *IEEE Trans. Instrum. Meas.* **56**, 592 (2007).
25. B. Andreas *et al.*, *Phys. Rev. Lett.* **106**, 030801 (2011).
26. T. J. Kippenberg, K. J. Vahala, *Science* **321**, 1172 (2008).
27. D. L. Freimund, H. Batelaan, *Phys. Rev. Lett.* **89**, 283602 (2002).

Acknowledgments: We thank S. Chu, P. Hamilton, and M. Kasevich for stimulating discussions; D. Budker, P. Kehaiyas, G. Kim, M. Xu, E. Ronayne Sohr, and D. Schlippert for experimental assistance; and A. Brachmann, R. Falcone, and W. E. White for providing a laser. J.M.B. acknowledges support by the Miller Institute for Basic Research in Science. This work was supported by the Alfred P. Sloan Foundation, the David and Lucile Packard Foundation, the National Institute of Standards and Technology, the National Science Foundation, and the National Aeronautics and Space Administration.

Supplementary Materials

www.sciencemag.org/cgi/content/full/science.1230767/DC1
Materials and Methods
Supplementary Text
Figs. S1 and S2
Table S1
References (*28*–*32*)

26 September 2012; accepted 20 November 2012
Published online 10 January 2013;
10.1126/science.1230767

Nanoscale Nuclear Magnetic Resonance with a Nitrogen-Vacancy Spin Sensor

H. J. Mamin,[1] M. Kim,[1,2] M. H. Sherwood,[1] C. T. Rettner,[1] K. Ohno,[3] D. D. Awschalom,[3] D. Rugar[1]*

Extension of nuclear magnetic resonance (NMR) to nanoscale samples has been a longstanding challenge because of the insensitivity of conventional detection methods. We demonstrated the use of an individual, near-surface nitrogen-vacancy (NV) center in diamond as a sensor to detect proton NMR in an organic sample located external to the diamond. Using a combination of electron spin echoes and proton spin manipulation, we showed that the NV center senses the nanotesla field fluctuations from the protons, enabling both time-domain and spectroscopic NMR measurements on the nanometer scale.

Both nuclear magnetic resonance (NMR) spectroscopy and magnetic resonance imaging (MRI) have become indispensable tools in many diverse fields of research, including analytical chemistry, materials science, structural biology, neuroscience, and medicine (*1*). The one major deficiency of NMR is the low sensitivity of the conventional coil-based induction method of detection, which prevents its application to samples at the nanometer scale (*2*). Much improved detection sensitivity has been achieved with magnetic resonance force microscopy, which is based on detecting weak magnetic forces in the presence of a strong field gradient and has demonstrated nanometer-scale NMR imaging at cryogenic temperatures (*3*). Here, we present an alternative nanoscale detection method that works in the absence of a magnetic field gradient, thus preserving spectroscopic information, and is operable over a wide range of temperatures, including room temperature. A single near-surface nitrogen-vacancy (NV) center in diamond is used as an atomic-size sensor to detect weak magnetic fields originating from nuclear spins external to the diamond. In an initial demonstration, we detected randomly polarized hydrogen nuclei (protons) in an organic polymer. Both time domain and spectroscopic information were obtained by appropriately manipulating the protons so as to affect the precession phase of the highly coherent NV electron spin. The results suggest that NV-based NMR detection may provide a path toward three-dimensional nanoscale magnetic resonance imaging (nanoMRI) under ambient conditions (*4*, *5*).

NV centers are proving to be particularly useful for both quantum information processing and nanoscale magnetic sensing (*6*–*11*). The negatively charged center has a spin state with a long coherence time, especially in isotopically purified crystals (*12*, *13*), and an electronic-level structure

[1]IBM Research Division, Almaden Research Center, San Jose, CA 95120, USA. [2]Center for Probing the Nanoscale, Stanford University, Stanford, CA 94305, USA. [3]Center for Spintronics and Quantum Computation, University of California, Santa Barbara, CA 93106, USA.

*To whom correspondence should be addressed. E-mail: rugar@us.ibm.com

that enables a convenient optical initialization and readout of the spin state. Much previous work has concentrated on the interactions of NV centers with nuclear spins internal to the diamond lattice (*14*–*17*), but nanoMRI requires the detection of external nuclear spins.

The key to effective external spin sensing is to have the NV center positioned near the diamond surface while maintaining a long spin coherence time (*18*–*20*). The spin coherence in diamond can be adversely affected by magnetic fluctuations from ^{13}C nuclear spins and various paramagnetic centers, such as nitrogen P1 centers and surface dangling bonds (*21*). In our experiments, the NV center was embedded in a layer of isotopically pure ^{12}C diamond grown epitaxially on top of an electronic grade (001)-oriented diamond substrate by plasma-enhanced chemical vapor deposition (Fig. 1A). NV centers were formed ~20 nm below the surface by briefly introducing $^{15}N_2$ gas during the growth process, followed by electron irradiation to create vacancies and annealing at 850°C to mobilize the vacancies and mitigate lattice damage (*13*, *22*). Despite their proximity to the surface, the resulting NV centers (Fig. 1B) had long electron spin coherence times T_{2e}, on the order of 600 μs as determined by Hahn spin echo measurements (Fig. 1D). This long spin coherence is critical for achieving the sensitivity required for these experiments.

The experimental apparatus consisted of a home-built scanning confocal microscope that uses 532-nm laser radiation to probe the NV center. Fluorescence from the NV center in the wavelength range of 600 to 800 nm was detected with an avalanche photodiode and gated photon counter. The fluorescence intensity is indicative of the NV spin state because the $m_s = 0$ spin state fluoresces with ~30% greater brightness than the $m_s = \pm 1$ states. To manipulate the spins in both the diamond and the polymer, a 3.6-μm-wide microwire was lithographically fabricated on the diamond surface and driven by a programmable microwave (MW) synthesizer for NV spin control and a radiofrequency (RF) function generator for proton spin control. The proton-containing sample was a 60-nm-thick layer of poly(methyl methacrylate) (PMMA) with proton density $\rho_N \approx 57$ nm^{-3} formed by spin casting on the diamond surface. A background magnetic field B_0 of 70 to 80 mT from a permanent magnet was accurately aligned to the NV symmetry axis (along the diamond [111] axis).

Several different protocols are possible for detecting weak magnetic signals from relatively distant nuclear spins. For the detection of internal ^{13}C nuclear spins, multipulse sequences, such as the Carr-Purcell-Meiboom-Gill (CPMG) sequence, have been used to selectively couple the NV center to the Larmor-frequency magnetic field emanating from freely precessing nuclei (*15*–*17*). This approach is effective when the nuclear spin precession has a T_{2n}^* correlation time comparable to or exceeding the electron spin coherence time T_{2e} of the NV center. By contrast, for a typical solid-state organic sample, the nuclear spin correlation time is greatly reduced by strong dipolar interactions among the densely packed protons. Conventional proton NMR measurements on our PMMA material found T_{2n} and T_{2n}^* to be 18 and 14 μs, respectively, much shorter than the 600-μs coherence time of the NV center. Thus, there is a mismatch in the time scales, and the nuclear spin precession will not remain coherent for the full duration of a long multipulse sequence (*20*). Rather than sensing the Larmor precession of the protons, we coupled the NV center to the longitudinal magnetization, which has a correlation time given by the spin-lattice relaxation time T_{1n}, on the order of seconds at room temperature.

As evident in Fig. 1C, the effective sample volume probed by the NV center was small, on the order of (24 nm)^3. Because of the small volume and low polarizing magnetic field, the proton polarization was dominated by $\sqrt{N}$ statistical fluctuations, where the number of protons N was of order 10^6 (*23*). Although the mean proton polarization was negligible, statistical fluctuations of the longitudinal polarization were detected by their effect on the phase of the NV spin precession (*20*, *24*–*27*). We started by polarizing the NV center to the $m_s = 0$ spin state with a 4-μs laser pulse (Fig. 2A). The NV center was then driven with MW pulses in a spin echo sequence with total echo time τ in the range of 300 to 440 μs. Synchronous with the spin echo sequence, we applied two identical RF pulses separated in time by τ/2, with each pulse consisting of exactly 30 sine wave cycles (approximating NMR π pulses). The first RF pulse set up an initial random longitudinal polarization for the first half of the echo sequence. The second RF pulse inverted this polarization for the second half. The inversion of proton polarization reversed the proton dipolar magnetic field $B_N(t)$ acting on the NV center and upset the equivalence of the NV spin precession for the two halves of the spin echo, thus reducing the spin echo amplitude. The identical nature of the RF pulses minimized any spurious effect they might have on the NV spin echo because identical disturbances during the two halves of the echo sequence should cancel. The spin echo sequence was typically repeated several million times to accumulate sufficient photon counting

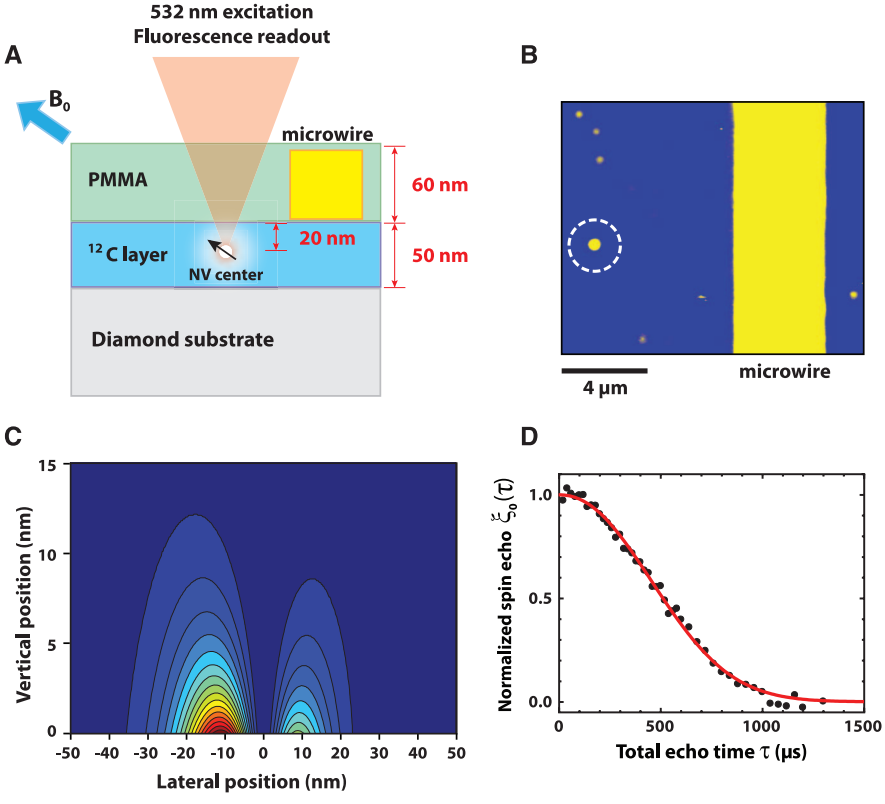

Fig. 1. Basic configuration of NV-NMR detection. (**A**) Sample geometry with [111]-oriented NV spin embedded 20-nm deep within ^{12}C diamond layer. The NV center detects NMR of protons in the PMMA polymer layer. (**B**) Fluorescence image of sample surface showing microwire and NV center (circled). (**C**) Cross-section of the PMMA layer showing calculated spatial dependence of proton detection sensitivity. Half of the proton signal originates from a volume of (24 nm)^3. The two lobes are a consequence of the 54.7° tilt angle of the NV axis with respect to the surface normal. (**D**) Normalized spin echo response versus total echo time. Solid curve is a fit of measured data points using the model $\xi_0(\tau) = \exp[-(\tau/T_{2e})^n]$. Fit parameters give $n = 2.17$ and $T_{2e} = 606$ μs.

statistics and to ensure that many different random polarization states of the sample protons were probed.

The spin echo response as a function of the frequency of the RF pulses (Fig. 2B) displayed distinct dips when the RF frequency matched the proton NMR frequency. As expected, the RF frequency for the dip depended on the magnitude of the applied static field B_0. The dip frequency as a function of field was well fit by a line with slope 42.6 MHz·T^{-1} (Fig. 2C), which matches the gyromagnetic ratio for protons. When the PMMA layer was removed from the diamond, the signal disappeared, indicating that the proton signal does indeed originate from the polymer and not from hydrogen contamination within the diamond (bottom curve in Fig. 2B).

The amplitude of the proton magnetic field fluctuations can be estimated from the depth of the dips in Fig. 2. The precession phase imbalance accumulated during the spin echo is given by $\delta\phi = \gamma\int_0^{\tau/2} B_N(t)dt - \gamma\int_{\tau/2}^{\tau} B_N(t)dt$, where $\gamma = 2\pi \times 28$ GHz·T^{-1} is the NV electron spin gyromagnetic ratio. Assuming $\delta\phi$ is a normally distributed random variable with zero mean, the resulting spin echo amplitude is $\xi(\tau) = \xi_0(\tau)\langle\cos\delta\phi\rangle = \xi_0(\tau)\exp(-\langle(\delta\phi)^2\rangle/2)$. Here, $\xi_0(\tau)$ is the normalized spin echo amplitude in the absence of proton reversals (Fig. 1D), $\langle\cdots\rangle$ indicates mean value, and $\langle(\delta\phi)^2\rangle$ is the variance of the accumulated phase, which depends on both the magnitude and correlation properties of the proton field fluctuations (*20*). For $T_{1n} >> \tau$, where $B_N(t)$ is essentially static for the duration of an individual echo sequence (except for the RF-induced inversion), $\langle(\delta\phi)^2\rangle = \gamma^2\tau^2\langle B_N^2\rangle$. Combining this equation with the expression for $\xi(\tau)$, we find $\langle B_N^2\rangle = (2/\gamma^2\tau^2)\log(\xi_0(\tau)/\xi(\tau))$, which simplifies for small fields to $\langle B_N^2\rangle = (2/\gamma^2\tau^2)\Delta\xi/\xi_0(\tau)$, where $\Delta\xi/\xi_0(\tau) = [\xi_0(\tau) - \xi(\tau)]/\xi_0(\tau)$ is the fractional change in spin echo amplitude.

The dips in Fig. 2B had depths that were roughly $\Delta\xi/\xi_0(\tau) = 0.20$, which from the above expressions

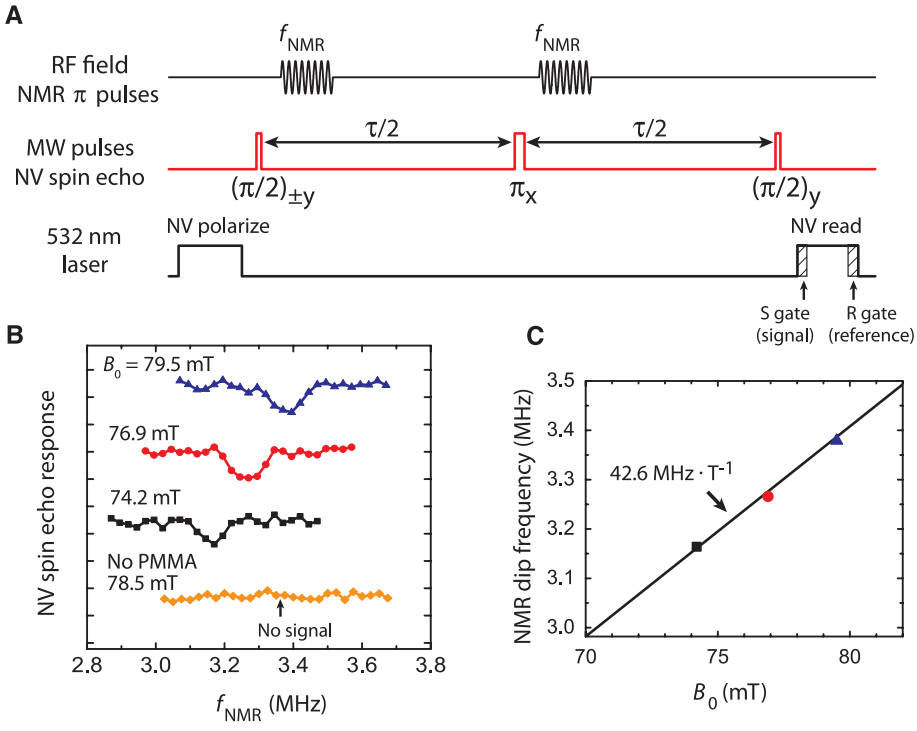

Fig. 2. Nanoscale NMR detection. (**A**) Pulsing scheme in which RF pulses serve to invert sample protons during the NV spin echo. Measurements are made with two different initial π/2 pulse phases. (**B**) Relative spin echo response as a function of RF frequency. With the PMMA sample present, clear dips are seen when the RF frequency matches the proton Larmor frequency. No dip is evident after PMMA has been removed. Curves are offset vertically for clarity. Total echo time was 300 μs. (**C**) Center frequency of dips versus external field B_0. Line shows expected dependence based on the proton gyromagnetic ratio.

Fig. 3. Time domain measurements and NMR spectrum taken at B_0 = 79.5 mT. (**A**) Spin echo sequence with an RF pulsing scheme similar to a Ramsey fringe. The effectiveness of proton inversion depends on evolution time τ_n. RF pulses consist of 15 sine wave cycles and approximate NMR π/2 pulses. (**B**) Proton-induced oscillation of spin echo response ξ as a function of τ_n measured in steps of 32 ns. The oscillation frequency matches the expected 3.38-MHz proton precession frequency. (**C**) Proton-induced oscillation of spin echo signal for a longer record where the sampling period is 336 ns. Undersampling of the waveform causes the apparent frequency to be shifted to 396 kHz due to aliasing. Initial decay during the first 15 μs is evident. (**D**) Solid curve: NV-based NMR spectrum obtained by cosine transform of data in (C). Frequencies have been shifted upward by 2.976 MHz to compensate for the aliasing effect. Dashed curve: Conventional 500-MHz NMR proton spectrum of PMMA that has been plotted to overlay the NV-based spectrum.

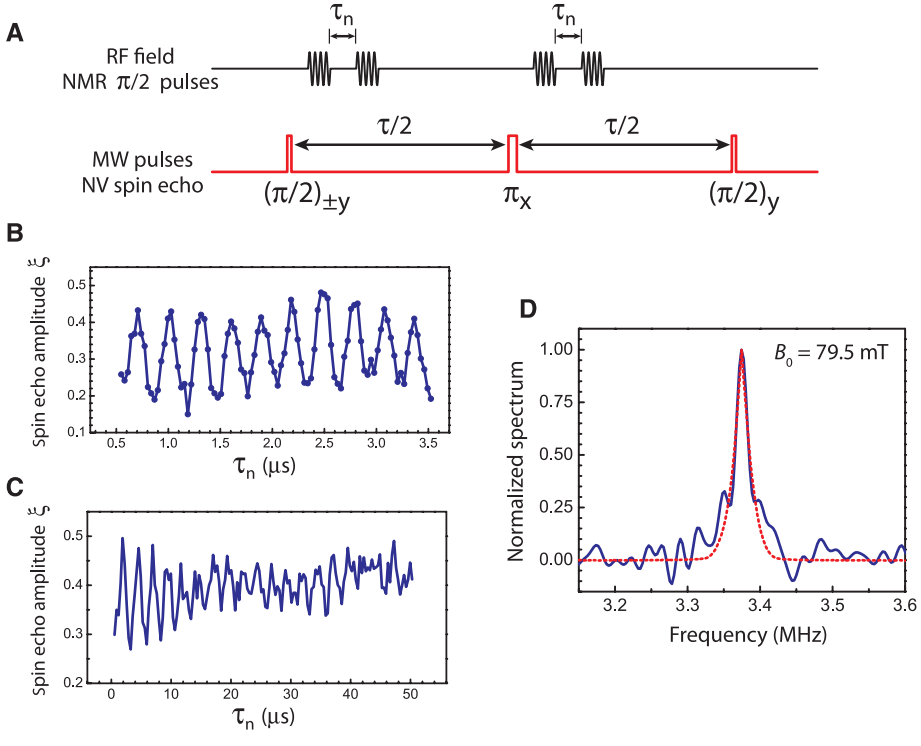

gives the root-mean-square magnetic field $B_{rms} \equiv \langle B_N^2 \rangle^{1/2} = 12$ nT-rms, a value substantially less than expected. For a thick polymer layer, the field was expected to be $B_{rms} \approx C\mu_0\mu_p\rho_N^{1/2}/d^{3/2}$, where $C = 1/8\sqrt{2\pi} \approx 0.050$, μ_0 is the permeability of free space, μ_p is the proton magnetic moment, and d is the depth of the NV center (*22*, *24*). Assuming a NV depth of 20 nm gives $B_{rms} = 75$ nT-rms, substantially greater than the experimental value. The cause of this discrepancy is not presently understood, but could be the result of greater-than-expected NV depth or inefficiency in the proton inversions by less-than-ideal RF field amplitude (estimated to be about 1 mT).

The signal-versus-frequency curves in Fig. 2B represent a crude form of NMR spectroscopy, but the dips are broadened by the amplitude of the RF pulses. To obtain higher spectral resolution, we implemented a Fourier transform technique resembling that used in conventional high-resolution NMR spectroscopy, where a time domain "free induction decay" (FID) is Fourier transformed to obtain the NMR frequency spectrum (*1*). We modified our pulse sequence by splitting each RF π pulse into a pair of π /2 pulses (Fig. 3A). We then incremented the spacing τ_n of the π /2 pulses in a manner similar to a Ramsey fringe experiment while monitoring the effect on the NV spin echo. This pulsing scheme differed from a conventional Ramsey experiment in that the frequency of the RF pulses was at the proton frequency and not at an offset frequency, and the RF pulses were not gated from a continuous-wave oscillator, but were triggered waveforms consisting of exactly 15 sine wave cycles.

As the pulse spacing τ_n was scanned, the NV spin echo response oscillated with a period that matched the proton Larmor frequency (Fig. 3B). This time domain response is roughly equivalent to a conventional FID in NMR, but is based on the correlation of the precession of the statistical proton polarization. No oscillations were seen if the RF frequency was far off the NMR resonance (e.g., by 600 kHz) or if the PMMA was removed (fig. S2).

To obtain a longer time record, we recorded the spin echo response using coarser steps in τ_n (Fig. 3C). The coarser steps allowed faster acquisition of a long time record, but undersampled the Larmor frequency oscillation, resulting in an "aliasing" effect where the Larmor precession frequency appeared to have shifted to a lower frequency. Despite the undersampling, the precession oscillations were clearly seen and decayed substantially during the first 15 μs, similar to the T_{2n}^* time scale expected for PMMA. After the initial decay, some oscillations persisted to the end of the 50-μs-long record, which was unexpected for a solid-state polymer given the short T_{2n}^*. This unexpected persistence of the apparent proton coherence is not understood, although it suggests that some component of the sample, perhaps residual solvent, has a longer than expected T_{2n}^*.

By applying a cosine transform to the time domain data, we obtained the frequency spectrum shown in Fig. 3D. The spectrum shows a single narrow peak at the proton Larmor frequency (after correcting for aliasing) with full width at half-maximum of ~20 kHz. Some broadening at the base of the peak is also evident. For comparison, we overlay a conventional NMR spectrum taken at 11.7 T, which also shows just a single central peak with a width that closely matches that of the NV-based spectrum.

The detection of external nuclear spins using a single NV center represents an important first step toward NV-based nanoMRI. Looking forward, it is instructive to evaluate current sensitivity levels and project possible improvements in the context of future imaging experiments. For the detection of the random fields with our protocol, the minimum detectable mean-square magnetic field [i.e., with unity signal-to-noise ratio (SNR)] is given by $B_{min}^2 = A/\gamma^2\tau^{3/2}T_a^{1/2}$, where T_a is the total acquisition time (*22*). The parameter A characterizes the photon-counting rate and spin-dependent contrast and is given by $A = 2\sqrt{2}(\alpha_0 + \beta_0)^{1/2}/(\alpha_0 - \beta_0)\xi_0(\tau)$, where α_0 and β_0 are the average number of photons detected per echo for the NV in the $m_s = 0$ and ±1 states, respectively. Under the present conditions of $\alpha_0 = 0.02$, $\beta_0 = 0.014$, $\tau = 440$ μs, and $\xi_0(\tau) = 0.60$, and assuming the longest practical dwell time for an imaging application to be $T_a = 60$ s, we find that $B_{min} = 8$ nT-rms.

Using the results of numerical calculations, we can interpret the minimum detectable field in terms of the volume of protons needed to produce such a field (*22*). Assuming a cubic volume element (voxel) located 20 nm above the NV center on the diamond surface, we find that the voxel size producing 8 nT-rms is $(4.3\ nm)^3$. Here, we have taken into account the 54.7° angle between the [111]-oriented spins and the (001) surface normal and assumed optimal lateral placement of the voxel. If we require a signal-to-noise ratio of 10, the corresponding volume element would be $(12\ nm)^3$. Many technical improvements in NV signal detection have been previously demonstrated that would enhance the spin sensitivity even further. For example, if we assume a fivefold improvement of fluorescence detection using microfabricated photonic structures (*18*, *28*) and a reduction of NV center depth to 5 nm with $T_{2e} = 200$ μs (*13*), we find that $B_{min} = 15$ nT-rms for a 60-s acquisition time. The reduced NV depth would greatly improve the sensitivity to the protons on the surface, yielding unity SNR for a volume element of only $(0.2\ nm)^3$, essentially single-proton sensitivity, if a (111)-oriented diamond surface is assumed. If we demand a SNR of 10 and require the ability to image at least 5 nm deep into the sample, the corresponding volume element is $(1.8\ nm)^3$. Although many technical issues still remain, the potential for three-dimensional nanoscale imaging with room-temperature operation, elemental selectivity, and no radiation damage suggests that NV-based nanoMRI could become an important complement to current state-of-the-art molecular imaging techniques, such as cryo-electron tomography (*29*) and noncontact atomic force microscopy (*30*).

References and Notes

1. R. R. Ernst, G. Bodenhausen, A. Wokaun, *Nuclear Magnetic Resonance in One and Two Dimensions* (Oxford Univ. Press, Oxford, 1987).
2. P. Glover, S. P. Mansfield, *Rep. Prog. Phys.* **65**, 1489 (2002).
3. C. L. Degen, M. Poggio, H. J. Mamin, C. T. Rettner, D. Rugar, *Proc. Natl. Acad. Sci. U.S.A.* **106**, 1313 (2009).
4. C. L. Degen, *Appl. Phys. Lett.* **92**, 243111 (2008).
5. B. M. Chernobrod, G. P. Berman, *J. Appl. Phys.* **97**, 014903 (2005).
6. A. Gruber *et al.*, *Science* **276**, 2012 (1997).
7. R. J. Epstein, F. M. Mendoza, Y. K. Kato, D. D. Awschalom, *Nat. Phys.* **1**, 94 (2005).
8. M. S. Grinolds *et al.*, *Nat. Phys.* **7**, 687 (2011).
9. F. Jelezko *et al.*, *Phys. Rev. Lett.* **93**, 130501 (2004).
10. J. R. Maze *et al.*, *Nature* **455**, 644 (2008).
11. G. Balasubramanian *et al.*, *Nature* **455**, 648 (2008).
12. G. Balasubramanian *et al.*, *Nat. Mater.* **8**, 383 (2009).
13. K. Ohno *et al.*, *Appl. Phys. Lett.* **101**, 082413 (2012).
14. P. Neumann *et al.*, *Science* **329**, 542 (2010).
15. N. Zhao *et al.*, *Nat. Nanotechnol.* **7**, 657 (2012).
16. T. H. Taminiau *et al.*, *Phys. Rev. Lett.* **109**, 137602 (2012).
17. S. Kolkowitz, Q. P. Unterreithmeier, S. D. Bennett, M. D. Lukin, *Phys. Rev. Lett.* **109**, 137601 (2012).
18. P. Maletinsky *et al.*, *Nat. Nanotechnol.* **7**, 320 (2012).
19. B. Grotz *et al.*, *New J. Phys.* **13**, 055004 (2011).
20. H. J. Mamin, M. H. Sherwood, D. Rugar, *Phys. Rev. B* **86**, 195422 (2012).
21. A. Laraoui, J. S. Hodges, C. A. Meriles, *Nano Lett.* **12**, 3477 (2012).
22. See supplementary materials on *Science* Online.
23. C. L. Degen, M. Poggio, H. J. Mamin, D. Rugar, *Phys. Rev. Lett.* **99**, 250601 (2007).
24. C. A. Meriles *et al.*, *J. Chem. Phys.* **133**, 124105 (2010).
25. A. Laraoui, J. Hodges, C. Ryan, C. Meriles, *Phys. Rev. B* **84**, 104301 (2011).
26. J. M. Taylor *et al.*, *Nat. Phys.* **4**, 810 (2008).
27. L. T. Hall, J. H. Cole, C. D. Hill, L. C. L. Hollenberg, *Phys. Rev. Lett.* **103**, 220802 (2009).
28. J. P. Hadden *et al.*, *Appl. Phys. Lett.* **97**, 241901 (2010).
29. E. I. Tocheva, Z. Li, G. J. Jensen, *Cold Spring Harb. Perspect. Biol.* **2**, a003442 (2010).
30. L. Gross, F. Mohn, N. Moll, P. Liljeroth, G. Meyer, *Science* **325**, 1110 (2009).

Acknowledgments: We thank F. Reinhard, J. Wrachtrup, P. Hemmer, and A. Bleszynski Jayich for helpful discussions. This work was supported by the Defense Advanced Research Projects Agency QuASAR program, the Air Force Office of Scientific Research, and the Center for Probing the Nanoscale at Stanford University (NSF grant PHY-0830228).

Supplementary Materials

www.sciencemag.org/cgi/content/full/339/6119/557/DC1
Materials and Methods
Supplementary Text
Figs. S1 to S3

15 October 2012; accepted 3 December 2012
10.1126/science.1231540